Optimisation of panel component regions subject to hot stamping constraints using a novel deep-learning-based platform

Optimisation of panel component regions subject to hot stamping constraints using a novel deep-learning-based platform

H R Attar[1], A Foster[2] and N Li[1,*]

[1] Dyson School of Design Engineering, Imperial College London, London SW7 2DB, UK
[2] Impression Technologies Ltd, Coventry CV5 9PF, UK
[*]Corresponding author, E-mail: n.li09@imperial.ac.uk

Abstract. The latest hot stamping processes can enable efficient production of complex shaped panel components with high stiffness-to-weight ratios. However, structural redesign for these intricate processes can be challenging, because compared to cold forming, the non-isothermal and dynamic nature of these processes introduces complexity and unfamiliarity among industrial designers. In industrial practice, trial-and-error approaches are currently used to update non-feasible designs where complicated forming simulations are needed each time a design change is made. A superior approach to structural redesign for hot stamping processes is demonstrated in this paper which applies a novel deep-learning-based optimisation platform. The platform consists of the interaction between two neural networks: a generator that creates 3D panel component geometries and an evaluator that predicts their post-stamping thinning distributions. Guided by these distributions the geometry is iteratively updated by a gradient-based optimisation technique. In the application presented in this paper, panel component geometries are optimised to meet imposed constraints that are derived from post-stamping thinning distributions. In addition, a new methodology is applied to select arbitrary geometric regions that are to be fixed during the optimisation. Overall, it is demonstrated that the platform is capable of optimising selective regions of panel component subject to imposed post-stamped thinning distribution constraints.

1. Introduction

The latest hot stamping processes are key enablers for realising vehicle lightweighting and therefore reducing use-phase emissions [1]. For example, the HFQ® process for high strength aluminium alloys developed by Lin *et al.* [2] improves material formability and addresses the springback issues of cold forming. Current research on these processes largely focuses on characterising the material behaviour under designed elevated temperature conditions to develop material constitutive models [3,4]. These models are to be embedded into high-fiedality finite element (FE) simulations to assess the stamping feasibility of designed panel components without actually producing a physical prototype, e.g. [5]. Nevertheless, these FE simulations occur late in design processes, as discussed in [6], require significant forming process and numerical experties, and are computationally expensive to evaluate. When coupled with the insufficient knoweldge that designers have of the latest hot stamping processes [6], the aforementioned challenges make finding optimum panel component geometries particularly difficult.

An effective alternative to iterative FE simulation runs is to employ surrogate-based numerical optimisation techniques. These techniques have been widely adopted in stamping applications for optimising scalar-based parameters, such as process parameters for fixed geometries, e.g., [7–9].

However, optimum process parameters cannot compensate for inadequately designed component geometries. Furthermore, unlike process parameters, geometries are significantly more complex and frequently evolving during design phases.

A deep-learning-based optimisation platform, recently developed by Attar *et al.* [10], opened the door to optimisation of arbitrary panel component geometries for stamping processes. Image-based surrogate models of a hot stamping process simulator (i.e., FE simulator) [11] were employed to rapidly assess the stamping performance of geometries that were being optimised. These surrogate models are agnostic to the geometry parameterisation as they process image-based representations of the design. Consequently, the geometric complexity is decoupled from the optimisation problem and a single predictive model can be trained with a large dataset of simulations that naturally accumulate in industrial settings. However, greater variation of geometries in the training dataset for the optimisation platform may result in the optimum geometry being significantly different from an initial geometry.

The purpose of this paper is to demonstrate novel engineering applications of the aforementioned optimisation platform [10] that extends its capability. Firstly, constraints on the thinning spatial gradients are introduced which explicitly regulate the post-stamping thickness uniformity during optimisation. Secondly, a new methodology is applied to selectively fix arbitrary regions of a panel component geometry to prevent them from changing during optimisation. These applications offer practical guidance for researchers and industrial engineers who are planning to use the platform to develop geometries that are optimised for stamping applications.

2. Overview of the optimisation platform

This section presents a high-level overview of the optimisation platform that was discussed in the introduction and presented in figure 1. For further details on the platform and neural network training and architectures, the reader is referred to the original paper by Attar *et al.* [10].

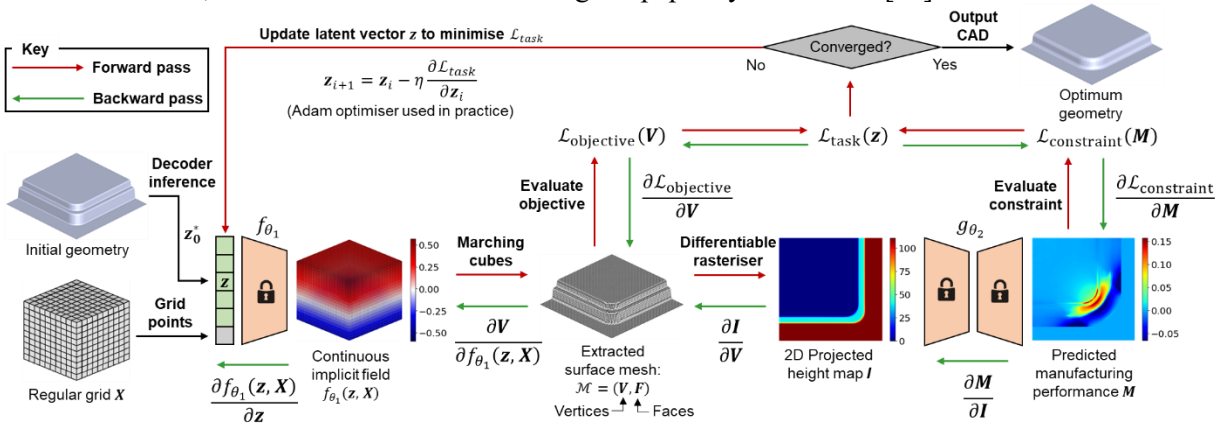

Figure 1. Optimisation platform overview. Symbols on f_{θ_1} and g_{θ_2} denote fixed network parameters.

The platform was based on the interaction of two pre-trained neural networks f_{θ_1} and g_{θ_2}. The former network f_{θ_1} took as input a latent vector $\boldsymbol{z}$ and a regular grid $\boldsymbol{X}$ of arbitrary resolution and generated a signed distance field (SDF) value [12], that was conditioned on $\boldsymbol{z}$, for every grid point $\boldsymbol{x} \in \boldsymbol{X}$. The generated SDF implicitly represented the geometry that was encoded in $\boldsymbol{z}$ by the zero-level-set of the SDF. Marching Cubes [13] was used to convert the zero-level-set into an explicit mesh-based representation of the geometry. The latter network g_{θ_2} took as input a 2D projected height map of this mesh and predicted the associated manufacturing performance distributions. Here, post-stamped thinning was the distribution considered. Further details on g_{θ_2} are given in Section 3.

The aim of the optimisation platform was to iteratively update the geometry (by updating $\boldsymbol{z}$) to minimise the function $\mathcal{L}_{\text{task}}$. This function was a summation of an objective function $\mathcal{L}_{\text{objective}}$ and a constraint function $\mathcal{L}_{\text{constraint}}$. These functions were task specific and were formulated based on the considered optimisation problem (see below). A forward pass through the platform occurred at each

optimisation iteration to compute $\mathcal{L}_{\text{task}}$ and update $\boldsymbol{z}$, as shown by the red arrows in figure 1. $\boldsymbol{z}$ was iteratively updated by the Adam optimiser [14] by using a variation of the simplified gradient descent shown in Equation (1) where the subscript i denotes the ith optimisation iteration and η is a constant.

$$\boldsymbol{z}_{i+1} = \boldsymbol{z}_i - \eta \frac{\partial \mathcal{L}_{\text{task}}}{\partial \boldsymbol{z}_i} \tag{1}$$

A backward pass occurred at each iteration, shown by the green arrows in figure 1, to compute $\partial \mathcal{L}_{\text{task}}/\partial \boldsymbol{z}$ to perform the $\boldsymbol{z}$ updates. The chain rule was used to compute $\partial \mathcal{L}_{\text{task}}/\partial \boldsymbol{z}$ as shown in Equation (2). Details on the computation of these gradients are given by Attar *et al*. [10].

$$\frac{\partial \mathcal{L}_{task}}{\partial \boldsymbol{z}} = \left(\frac{\partial \mathcal{L}_{objective}}{\partial \boldsymbol{V}} + \frac{\partial \mathcal{L}_{constraint}}{\partial \boldsymbol{M}} \cdot \frac{\partial \boldsymbol{M}}{\partial \boldsymbol{I}} \cdot \frac{\partial \boldsymbol{I}}{\partial \boldsymbol{V}} \right) \cdot \frac{\partial \boldsymbol{V}}{\partial f_{\theta_1}(\boldsymbol{z}, \boldsymbol{X})} \cdot \frac{\partial f_{\theta_1}(\boldsymbol{z}, \boldsymbol{X})}{\partial \boldsymbol{z}} \tag{2}$$

3. Manufacturing performance evaluator model

An overview of the manufacturing performance evaluator model g_{θ_2} is presented and further details can be found by Attar *et al*. [11,15]. This model was a CNN based surrogate of the HFQ process [2] and was able to predict the post-stamped thinning distribution associated with an input die geometry.

3.1. Geometry definitions

The geometries considered in this study were two subclasses of deep drawn box corners. These subclasses were parameterised individually and are presented in figure 2. Using these parametric models together with the Latin Hypercube design of experiments technique [16], 1000 CAD variants of these geometries were generated and prepared for the subsequent forming simulations.

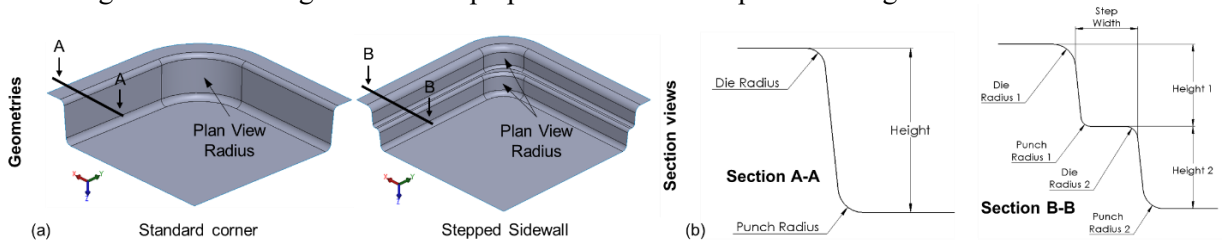

Figure 2. Parametric models of two symmetric deep drawn box corner geometry subclasses (standard corners and stepped sidewalls) considered in this study. (a) 3D CAD views with labelled corner parameters and (b) section views with labelled sidewall parameters. Box half side length was 500 mm for all geometries.

3.2. HFQ forming simulations

Forming simulations were required to generate the post-stamping thinning distributions that were associated with each CAD geometry variant. These distributions were used as the targets for the training and testing data for g_{θ_2}. Non-isothermal simulations of the HFQ forming process [2] were conducted in PAM-STAMP. The Python programming language was used to automate the meshing and loading of each geometry variant into PAM-STAMP and launch the simulations. The processing parameters were kept constant and set according to [10]. The temperature and strain rate dependent material model for AA6082 under HFQ conditions which was presented in [17] was used.

3.3. Model overview

The Res-SE-U-Net image-based architecture [11,15] was used for g_{θ_2} and an overview of the manufacturability assessment technique using this model is presented in figure 3. The model was trained on 2D height map images of the input geometries and corresponding 2D thinning distributions plotted on the undeformed blank shape that were pre-processed from the forming simulation results.

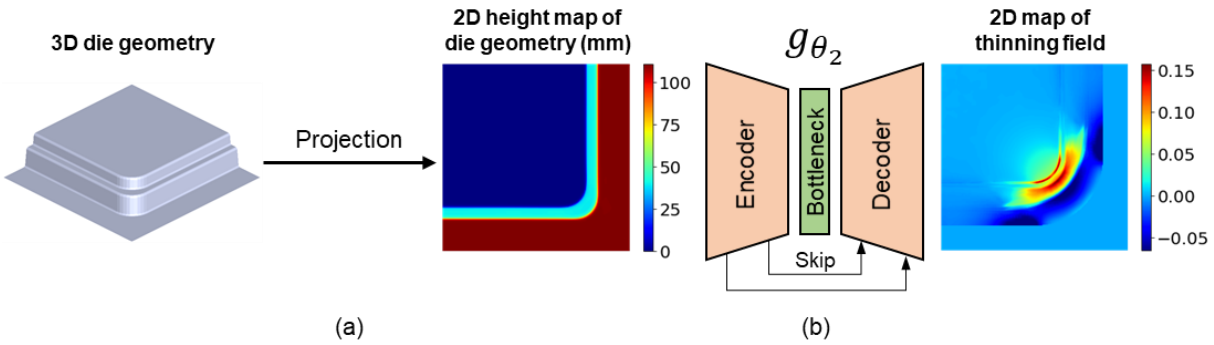

Figure 3. Overview of the manufacturing performance assessment approach. (a) 2D projection of 3D die geometry. (b) Thinning field prediction using CNN based surrogate model given the input height map.

To predict the manufacturing performance of a geometry that was being optimised, a 2D projection was first performed to obtain its height map, shown in figure 3(a). The 2D projection was possible without information loss since stamping geometries must be undercut-free to avoid collision with the forming tools. The projection was performed by the differentiable rasteriser available from the PyTorch3D python library [18]. The output of g_{θ_2} was a predicted post-stamped thinning distribution that was plotted on the 2D undeformed blank shape, shown in figure 3(b).

3.4. Manufacturability constraints

Two manufacturability constraints were formulated based on the predicted thinning distribution and were used to define $\mathcal{L}_{\text{constraint}}$ for the optimisation platform, as shown in Equation (3).

$$\mathcal{L}_{\text{constraint}} = \lambda_1 \text{ReLU}\big(\max\big(\boldsymbol{M}(\boldsymbol{z})\big) - t_{\max}\big) + \lambda_2 \text{ReLU}(\max(\|\nabla \boldsymbol{M}(\boldsymbol{z})\|_2^*) - t'_{\max}) \quad (3)$$

The first and second terms were concerned with imposed constraints on the maximum thinning $t_{\max}$ level and maximum thinning spatial gradient level $t'_{\max}$ respectively and the λ terms were weighting scalars. The function $\text{ReLU}(x) := \max(0, x)$ was used in Equation (3) to make each of the two terms in $\mathcal{L}_{\text{constraint}}$ inactive when their $\max(\cdot)$ terms were below their set constraint level ($t_{\max}$ or $t'_{\max}$) and active otherwise. $\boldsymbol{M}(\boldsymbol{z})$ is the predicted post-stamping thinning field defined as in Equation (4)

$$\boldsymbol{M}(\boldsymbol{z}) = g_{\theta_2}\left(\phi\left(f_{\theta_1}(\boldsymbol{z}, \boldsymbol{X})\right)\right) \quad (4)$$

where ϕ is the combined marching cubes [13] and differentiable rasteriser [18] steps in figure 1. Here, ϕ can be thought of as a differentiable function that converts the volumetric SDF $f_{\theta_1}(\boldsymbol{z}, \boldsymbol{X})$ into a 2D height map of the geometry encoded in $\boldsymbol{z}$. $\|\nabla \boldsymbol{M}(\boldsymbol{z})\|_2^*$ is the masked norm of the spatial gradient (i.e., in the x and y directions) of the generated 2D thinning field and defined as in Equation (5).

$$\|\nabla \boldsymbol{M}(\boldsymbol{z})\|_2^* = mask\left(\sqrt{\left(\frac{\partial \boldsymbol{M}(\boldsymbol{z})}{\partial \boldsymbol{x}}\right)^2 + \left(\frac{\partial \boldsymbol{M}(\boldsymbol{z})}{\partial \boldsymbol{y}}\right)^2}\right) \quad (5)$$

Figure 4 shows an illustration of $\|\nabla \boldsymbol{M}\|_2^*$. To obtain $\|\nabla \boldsymbol{M}\|_2^*$, the spatial gradient of the predicted thinning distribution in figure 4(a) was calculated to obtain the distribution in figure 4(b). To eliminate false areas of thinning gradient (for example at the border of the blank shape in figure 4(b)), the distribution was masked by setting pixel values corresponding to thinning < 0 to zero. The constraint on the maximum thinning gradient was used to constrain the thickness uniformity due to thinning. As an intuitive example, consider superplastic forming [19] where large values of maximum thinning may be deemed acceptable if spread across a large enough area.

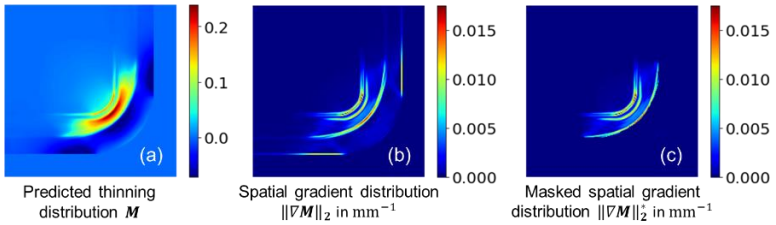

Figure 4. Illustration of a thinning distribution that was predicted from g_{θ_2} and its spatial gradients.

4. Design optimisation

This section presents details on two optimisation tasks that were performed using the optimisation platform that was presented in figure 1.

4.1. Optimisation Task 1

4.1.1. Task description. Task 1 was to optimise the initial stepped sidewall geometry shown in figure 5(b)(top). The objective function $\mathcal{L}_{objective}$ of task 1 was formulated according to Equation (6).

$$\mathcal{L}_{\text{objective}} = \frac{\lambda_3}{|\boldsymbol{z}|}\|\boldsymbol{z}_0 - \boldsymbol{z}\|_2^2 + \lambda_4|H - H_{\text{ref}}| \tag{6}$$

The first term was a latent similarity loss and the second term was a height loss, and the λ terms were weighting scalars. The former was formulated in terms of the latent vectors $\boldsymbol{z}_0$ (which was constant) and $\boldsymbol{z}$ which were vector representations of the initial geometry and geometry being optimised, respectively. Details on $\boldsymbol{z}_0$ are given by Attar *et al.* [10]. Minimising this similarity loss ensured that the optimum geometry had geometric features that closely resemble the ones of the initial geometry (e.g., maintaining the stepped sidewall). Minimising height loss ensured that the height of the geometry being optimised H was as close as possible to a reference height H_{ref}. Here, H_{ref} was taken to be the height of the initial geometry and was 110 mm. The $t_{\max}$ and $t'_{\max}$ constraints were set to 0.1 and 0.0075 mm^{-1} respectively and were used to formulate $\mathcal{L}_{\text{constraint}}$ in Equation (3).

4.1.2. Optimisation results and discussion. The results of task 1 are shown in figure 5 and the history is plotted in figure 5(a). The maximum thinning steadily decreased from 0.24 to the set constraint level of 0.1 in the first 340 iterations. The maximum thinning gradient decreased from 0.0145 mm^{-1} to below the set constraint level of 0.0075 mm^{-1} in the first 245 iterations. Consequently, at iteration 340, both constraints were inactive according to Equation (3). After iteration 340, the remainder of the optimisation was driven by minimising the latent similarity and height losses while satisfying the constraints. A relatively large value of λ_4 was used in the objective function (see Equation (6)) to enforce the recovery of the desired height of 110 mm at the end of the optimisation. Concurrently, the radii geometric featured became larger to accommodate the height gain and this resulted in the latent similarity loss increasing from iteration 650 onwards.

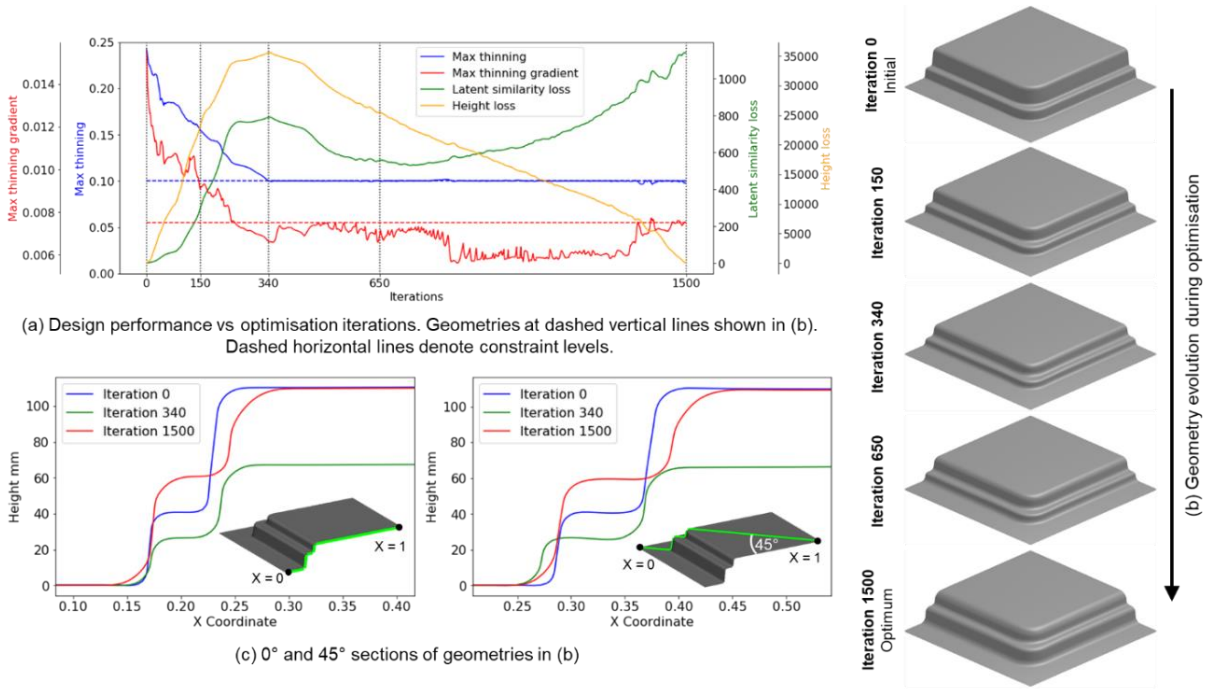

Figure 5. Optimisation task 1 results.

4.2. Optimisation Task 2

4.2.1. Task description. The optimisation performed in task 1 enabled the entire geometry to change. In contrast, task 2 was to optimise the initial stepped sidewall geometry shown in figure 7 while keeping selective geometric regions fixed. The objective function $\mathcal{L}_{objective}$ to be minimised was formulated to penalise geometric deviations from the regions to be fixed. The procedure for measuring these geometric deviations and computing $\mathcal{L}_{objective}$ is summarised in figure 6. An example case for fixing the top 50 mm of the initial geometry is shown for illustration, but the same procedure can be applied for fixing any arbitrary geometric region (for example, in figure 7).

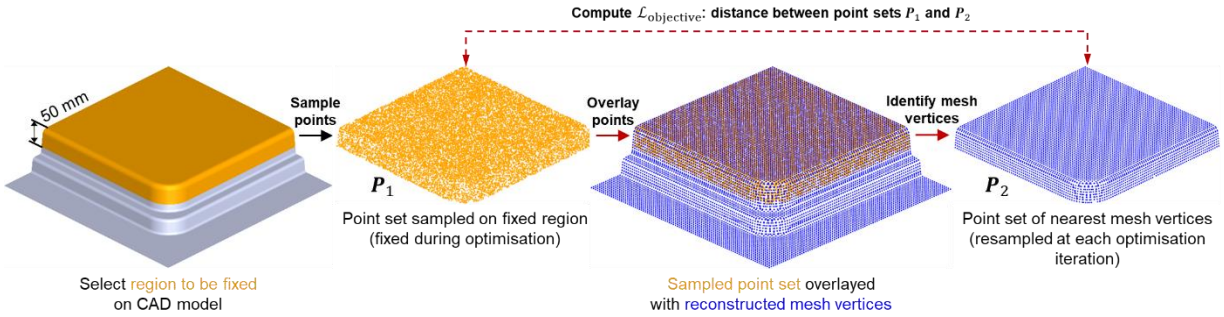

Figure 6. Procedure for measuring the geometric deviations from a region to be fixed during optimisation. Example case for fixing the top 50 mm is shown. Red arrows occur once per optimisation iteration. Blue points are vertices of the reconstructed mesh that was the output of Marching Cubes (see figure 1).

The surfaces for a region to be fixed were first selected on the CAD model and sampled with points using functionality from the PyTorch3D library [18]. These points are shown by the orange point set in figure 6 and denoted as $\boldsymbol{P}_1$ and were fixed during optimisation. At each optimisation iteration, these points were overlayed with vertices of the reconstructed mesh that was the output of Marching Cubes

(see figure 1). To identify the nearest mesh vertices, a search was performed to find all mesh vertices within a small radius r = 8 mm of every point in $\boldsymbol{P}_1$ and any duplicates were removed. In practice, this search was efficiently performed using a KD-tree from the SciPy library [20]. The identified mesh vertices are shown by the blue point set $\boldsymbol{P}_2$ in figure 6(right). The chamfer distance between $\boldsymbol{P}_1$ and $\boldsymbol{P}_2$, weighted by the scalar λ_5, was set as the objective function $\mathcal{L}_{\text{objective}}$ according to Equation (7). Minimising this function promoted the two point sets, and therefore the surfaces that they were sampled from, to be as close as possible (i.e., fixed since $\boldsymbol{P}_1$ does not change) during optimisation.

$$\mathcal{L}_{\text{objective}} = \lambda_5 \left(\sum_{\boldsymbol{x}_i \in \boldsymbol{P}_1} \min_{\boldsymbol{x}_j \in \boldsymbol{P}_2} \left\| \boldsymbol{x}_i - \boldsymbol{x}_j \right\|_2^2 + \sum_{\boldsymbol{x}_j \in \boldsymbol{P}_2} \min_{\boldsymbol{x}_i \in \boldsymbol{P}_1} \left\| \boldsymbol{x}_i - \boldsymbol{x}_j \right\|_2^2 \right) \tag{7}$$

Two cases for task 2 were considered in this study, both using the same initial geometry but with different regions to be fixed during optimisation, as shown in figure 7. The unselected regions shown in grey in figure 7 were free to change during optimisation to meet the manufacturing constraints.

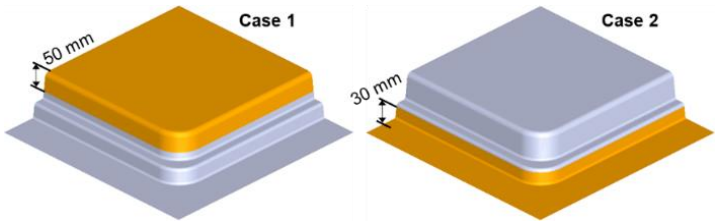

Figure 7. Fixed geometry regions shown in orange. Top 50 mm fixed for case 1 and bottom 30 mm fixed for case 2.

The constraints on maximum thinning $t_{\max}$ and maximum thinning gradient $t'_{\max}$ were set to 0.15 and 0.01 mm^{-1} respectively for case 1, and 0.1 and 0.0075 mm^{-1} respectively for case 2 and were used to formulate $\mathcal{L}_{\text{constraint}}$ in Equation (3).

4.2.2. Optimisation results and discussion. The results of these cases 1 and 2 for this optimisation task are shown in figure 8 and figure 9 respectively. Similar to task 1, the maximum thinning and maximum thinning gradient fell below the set manufacturing constraints during optimisation. For both cases, the chamfer loss in Equation (7) remained approximately constant, which suggests that the regions to be fixed did not change during optimisation. This suggestion was confirmed when viewing the geometry evolutions during optimisation, seen in figures (b) and by viewing the sectional views in figures (c). Particularly for case 2, the stepped feature was removed and transitioned into a standard corner in order to maintain the tight radii in the fixed region. Overall, it was seen that the proposed methodology enabled selective geometric regions to be fixed during optimisation.

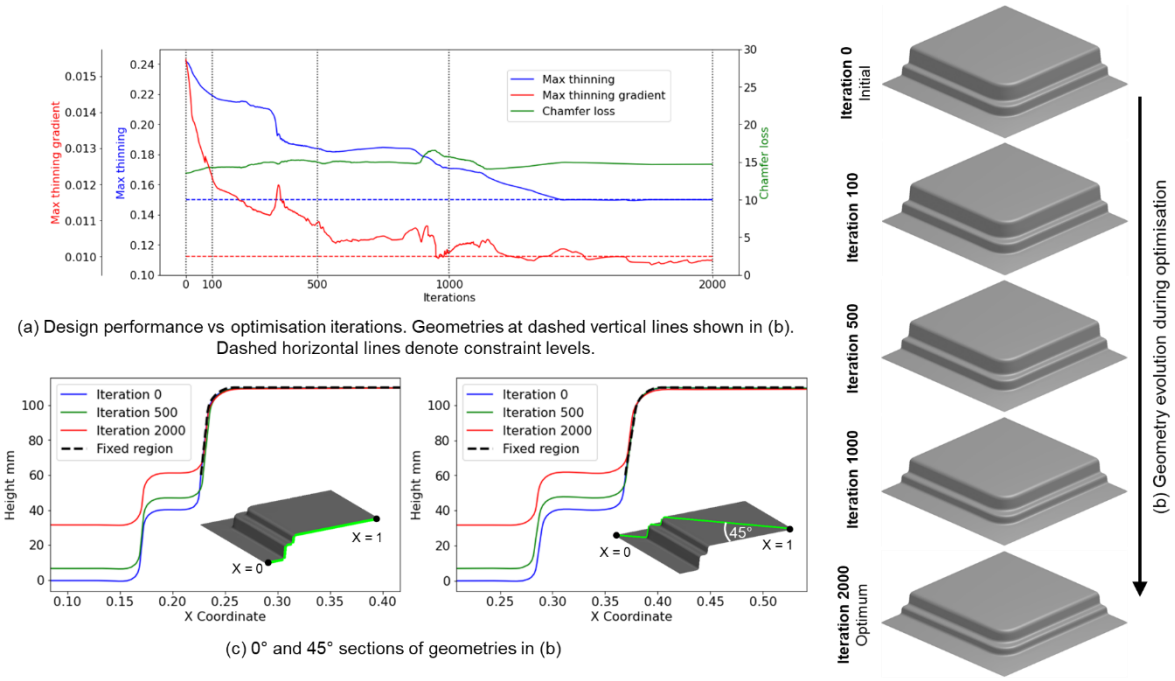

Figure 8. Optimisation task 2 results: case 1.

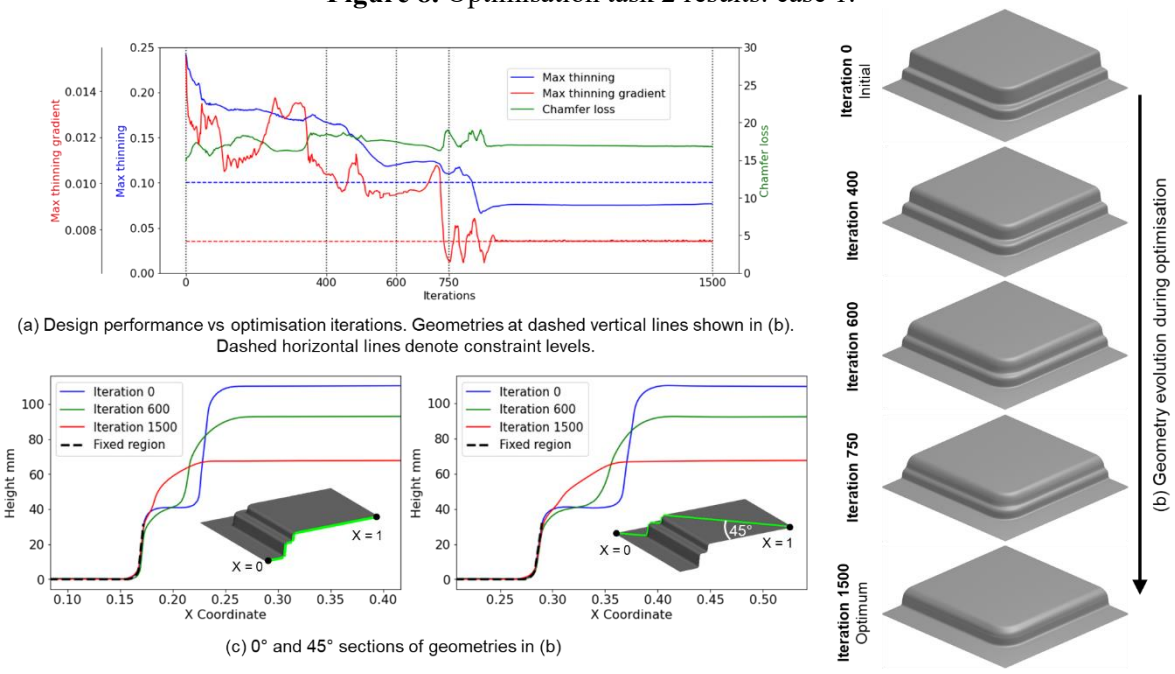

Figure 9. Optimisation task 2 results: case 2.

5. Conclusion

Novel applications of a deep-learning-based platform for iteratively optimising panel component geometries subject to hot stamping performance constraints were presented. The platform consisted of the interaction between two neural networks: a generator that created 3D panel component geometries and an evaluator that predicted their post-stamping thinning distributions. Based on these distributions, a constraint function was formulated that enabled both constraints on maximum thinning and maximum thinning spatial gradient to be incorporated into the geometric optimisation procedure. In

addition, a new methodology was applied to select arbitrary geometric regions, as desired design features to be kept unchanged, during optimisation. Based on this methodology, an objective function was formulated to penalise deviations from these selected regions. Overall, it was demonstrated that geometric changes that are driven by both maximum thinning and maximum thinning gradient are possible using the optimisation platform. It was further demonstrated that selective panel component regions can be fixed during optimisation while the rest of the geometry was free to be optimised. The applications presented here offer practical guidance for researchers and engineers who are planning to use the platform to develop optimum panel component geometries for stamping processes.

References

[1] Raugei M, El O, Wang L, Lin J and Morrey D 2014 Life cycle assessment of the potential environmental benefits of a novel hot forming process in automotive manufacturing *J. Clean. Prod.* **83** 80–6
[2] Lin J, Dean T A, Garrett R P and Foster A D 2008 Process for forming aluminium alloy sheet component
[3] Mohamed M S, Foster A D, Lin J, Balint D S and Dean T A 2012 Investigation of deformation and failure features in hot stamping of AA6082: Experimentation and modelling *Int. J. Mach. Tools Manuf.* **53** 27–38
[4] Shao Z, Li N, Lin J and Dean T 2017 Formability evaluation for sheet metals under hot stamping conditions by a novel biaxial testing system and a new materials model *Int. J. Mech. Sci.* **120** 149–58
[5] El Fakir O, Wang L, Balint D, Dear J P, Lin J and Dean T A 2014 Numerical study of the solution heat treatment, forming, and in-die quenching (HFQ) process on AA5754 *Int. J. Mach. Tools Manuf.* **87** 39–48
[6] Attar H R, Li N and Foster A 2021 A new design guideline development strategy for aluminium alloy corners formed through cold and hot stamping processes *Mater. Des.* **207**
[7] Zhou J, Wang B, Lin J and Fu L 2013 Optimization of an aluminum alloy anti-collision side beam hot stamping process using a multi-objective genetic algorithm *Arch. Civ. Mech. Eng.* **13** 401–11
[8] Huang M D, Li C, Fu L, Li L and Liu C 2018 Stamping parameters optimization of an AA5754 A-pillar by response surface methodology *J. Phys. Conf. Ser.* **1063** 1–7
[9] Ma Z, Ji H, Huang X, Xiao W and Tang X 2021 Research on high temperature stamping forming performance and process parameters optimization of 7075 aluminum alloy *Materials (Basel).* **14** 1–23
[10] Attar H R, Foster A and Li N 2022 Development of a deep learning platform for optimising sheet stamping geometries subject to manufacturing constraints *arXiv*
[11] Attar H R, Zhou H, Foster A and Li N 2021 Rapid feasibility assessment of components to be formed through hot stamping : A deep learning approach *J. Manuf. Process.* **68** 1650–71
[12] Park J J, Florence P, Straub J, Newcombe R and Lovegrove S 2019 DeepSDF: Learning continuous signed distance functions for shape representation *arXiv*
[13] Lorensen W E and Cline H E 1987 Marching cubes: A high resolution 3D surface construction algorithm *Proc. 14th Annu. Conf. Comput. Graph. Interact. Tech. SIGGRAPH 1987* **21** 163–9
[14] Kingma D P and Ba J L 2015 Adam: A method for stochastic optimization *3rd Int. Conf. Learn. Represent. ICLR 2015 - Conf. Track Proc.* 1–15
[15] Attar H R, Zhou H and Li N 2021 Deformation and thinning field prediction for HFQ® formed panel components using convolutional neural networks *IOP Conf. Ser. Mater. Sci. Eng.* **1157** 012079
[16] Bonte M H, van den Boogaard A and Huétink J 2007 A metamodel based optimisation algorithm for metal forming processes *Adv. Methods Mater. Form.*
[17] El Fakir O 2015 *Studies on the Solution Heat Treatment , Forming and in-Die Quenching Process in the Production of Lightweight Alloy Components* (Imperial College London)

[18] Ravi N, Reizenstein J, Novotny D and Gordon T 2020 Accelerating 3D deep learning with PyTorch3D *arXiv*
[19] Zheng K, Politis D J, Wang L and Lin J 2018 A review on forming techniques for manufacturing lightweight complex—shaped aluminium panel components *Int. J. Light. Mater. Manuf.* **1** 55–80
[20] SciPy 2022 SciPy documentation

Acknowledgments
The authors thank Impression Technologies Ltd for funding support and the UK EPSRC for the CASE conversion DTP training grant (EP/R513052/1). Software from ESI Group is gratefully acknowledged.